Supplement of Atmos. Chem. Phys., 26, 4439–4451, 2026
https://doi.org/10.5194/acp-26-4439-2026-supplement
© Author(s) 2026. CC BY 4.0 License.

Atmospheric Chemistry and Physics
Open Access
EGU

Supplement of

The effect of organic nucleation on the indirect radiative forcing with a semi-explicit chemical mechanism for highly oxygenated organic molecules (HOMs)

Xinyue Shao et al.

Correspondence to: Minghuai Wang (minghuai.wang@nju.edu.cn) and Xinyi Dong (dongxy@nju.edu.cn)

The copyright of individual parts of the supplement might differ from the article licence.

Text S1. Description of the Newly Added Chemical Mechanisms

Figure S1 shows a flowchart of the HOMs mechanism implemented into CAM6-Chem and Table S1 shows the main chemical reactions added into CAM6-Chem. In general, monoterpenes (including α-pinene, β-pinene, limonene and myrcene) are oxidized by OH radicals or O_3 to form MT-aRO_2 and MT-bRO_2 radicals (reactions 1-2 listed in Table S1, with only reactions involving α-pinene shown as an example). MT-bRO_2 undergo multi-step autoxidation reactions to form HOMs with 10 carbon atoms (C10-HOMs) (green arrows in Fig. S1 and reactions 3-4 in Table S1). The intermediates for the autoxidation are MT-cRO_2 and MT-HOM-RO_2. The MT-HOM-RO_2 radical represents the RO_2 radicals that undergo two or multi-step autoxidation. On the one hand, MT-HOM-RO_2 radicals are further oxidized to form C10-HOMs (reaction 8-10 in Table S1). On the other hand, all the MT-RO_2 radicals (including MT-aRO_2, MT-bRO_2, MT-cRO_2, and MT-HOM-RO_2) undergo self- and cross-reactions (orange arrows in Fig. S1) to form accretion products (C15 and C20) (reactions 5-7 in Table S1, with only reactions involving MT-aRO_2 shown as an example). The formation processes of C10-HOMs can be terminated by several oxidants (gray arrows in Fig. S1). SOA is formed via gas-particle partitioning processes of C10-HOMs, C15 and C20 (blue dashed arrows in Fig. S1).

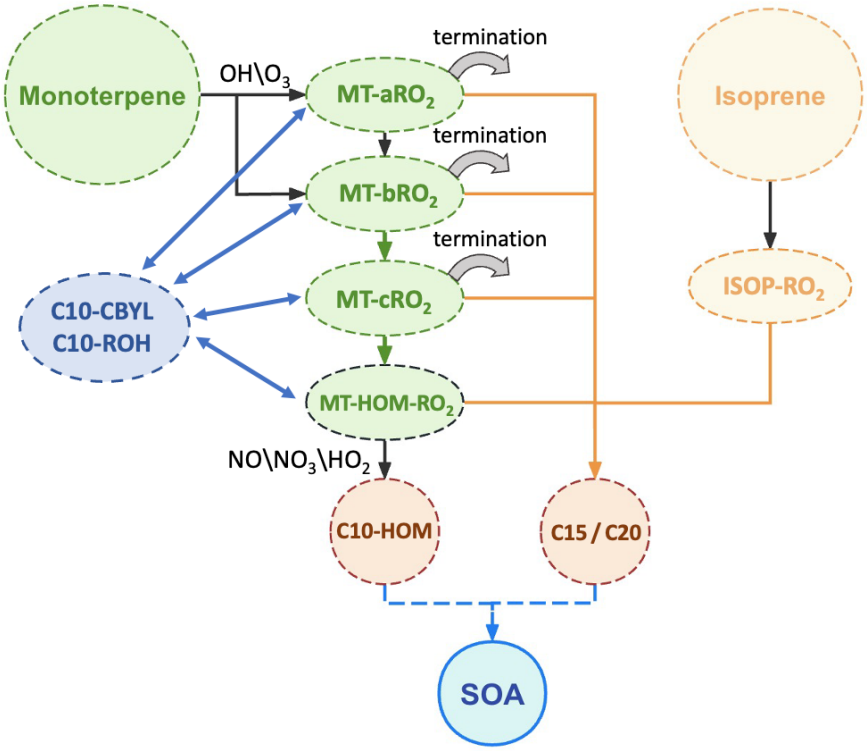

Figure S1. The flow chart of the formation and gas-particle partitioning processes of HOMs and accretion products. The green arrows represent the autoxidation reactions. The gray curved solid arrows represent the termination reactions. The yellow arrows represent the self- and cross-reactions. The blue arrows represent the conversion between C10-CBYL\C10-ROH and MT-RO2 radicals. The blue dashed arrows represent the gas-particle partitioning processes.

Table S1. Main chemical reactions added in CAM6-Chem

Index	Reactions
1	APIN + OH → 0.25*$APINO_2$ + 0.75*MT-bRO_2
2	APIN + O_3 → 0.736*$APINO_2$ + 0.064*MT-bRO_2 + 0.77*OH + 0.066*$TERPA2O_2$ + 0.22*H_2O_2 + 0.044*TERPA + 0.002*TERPACID + 0.034*TERPA2 + 0.17*HO_2 + 0.17*CO + 0.27*CH_2O + 0.054*$TERPA2CO_3$
3	MT-bRO_2 → MT-cRO_2
4	MT-cRO_2 → MT-HOM-RO_2
5	MT-aRO_2 + MT-aRO_2 → 0.893*C_{10}-CBYL + 0.29*C_{10}-ROH + 0.603*HO_2 + 1.34*HYDRALD + 0.067*MT-bRO_2 + 0.04*SOAGac20
6	MT-aRO_2 + MT-bRO_2 → 0.96*C_{10}-CBYL + 0.29*C_{10}-ROH + 0.67*HO_2 + 1.34*HYDRALD + 0.04*SOAGac20
7	MT-aRO_2 + ISOP-RO_2 → 0.4465*C_{10}-CBYL + 0.145*C_{10}-ROH + 0.145*ROH + 0.603*HO_2 + 1.485*HYDRALD + 0.0335*MT-bRO_2 + 0.04*SOAGac15
8	MT-HOM-RO_2 + HO_2 → SOAGhma + O_2
9	MT-HOM-RO_2 + NO → 0.8*NO_2 + 0.8*HO_2 + 0.4*SOAGhmb + 0.8*HYDRALD + 0.2*SOAGhmn
10	MT-HOM-RO_2 + NO_3 → HO_2 + NO_2 + 0.5*SOAGhmb + HYDRALD

Table S2. Species for HOMs and ACC formation mechanism.

Species	Molecular formula	Description
APIN [b]	$C_{10}H_{16}$	α-pinene
$APINO_2$ [b]	$C_{10}H_{17}O_3$	peroxy radical from OH +α-pinene reaction
MT-bRO_2 [a]	$C_{10}H_{16}O_4$	RO_2 from monoterpene+O_3/OH that can undergo autoxidation
MT-cRO_2 [a]	$C_{10}H_{16}O_6$	RO_2 from MT-bRO_2 autoxidation
MT-HOM-RO_2 [a]	$C_{10}H_{16}O_8$	RO_2 from MT-cRO_2 autoxidation
SOAGhma [a]	$C_{10}H_{14}O_9$	gas-phase C10 HOMs product without nitrate from HO_2 reaction
SOAGhmb [a]	$C_{10}H_{14}O_9$	gas-phase C10 HOMs product without nitrate from NO and NO_3 reaction
SOAGhmn [a]	$C_{10}H_{14}O_9N$	gas-phase C10 HOMs product with nitrate from NO reaction
SOAGac15 [a]	$C_{15}H_{18}O_7$	gas-phase C15 accretion product from isoprene-derived RO_2 (ISOP-RO_2) + MT-RO_2
SOAGac20 [a]	$C_{20}H_{32}O_8$	gas-phase C20 accretion product from MT-RO_2 + MT-RO_2
ROH [a]	C_3H_8O	lumped alcohols with more than 2 carbons
C_{10}-CBYL [a]	$C_{10}H_{17}O_3$	Carbonyl with 10 carbon atoms
C_{10}-ROH [a]	$C_{10}H_{17}O_3$	Alcohol with 10 carbon atoms
CH_2O [b]	CH_2O	formaldehyde
HO_2 [b]	HO_2	hydroperoxyl radical
H_2O_2 [b]	H_2O_2	hydrogen peroxide
HYDRALD [b]	$HOCH_2CCH_3CHCHO$	lumped unsaturated hydroxycarbonyl
TERPA [b]	$C_{10}H_{16}O_2$	aldehyde terpene product with no double bonds that contains a ring like pinonaldehyde
TERPACID [b]	$C_{10}H_{16}O_4$	carboxylic acid/peracid from TERPA
TERPA2 [b]	$C_9H_{14}O_2$	TERPA oxidation product with no double bonds that contains an aldehydic group
TERPA2O_2 [b]	$C_9H_{15}O_4$	TERPA peroxy radical 2nd step
TERPA2CO_3 [b]	$C_9H_{13}O_4$	acyl peroxy radical from TERPA2

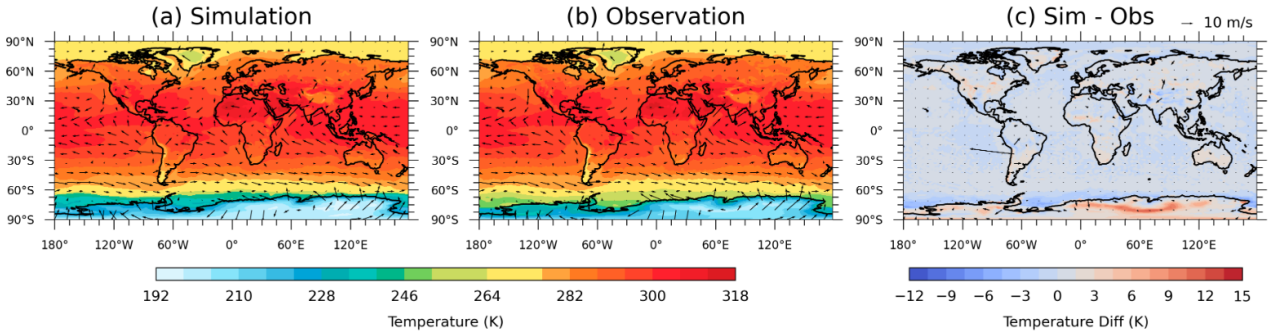

Figure S2. Spatial distribution of (a) simulated and (b) observed temperature (shaded, unit: K) and wind speed (arrows, unit: m s^{-1}). Panel (c) shows the difference in temperature between simulation and observation.

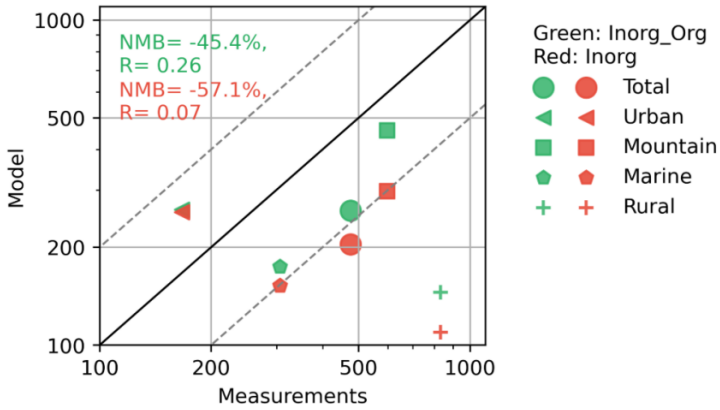

Figure S3. Comparison of simulated monthly mean and observed median CCN number concentrations (unit: cm^{-3}) at categorized background sites. Results from the Inorg_Org experiment are shown in green, and those from the Inorg experiment are shown in red. Information on the measurement sites is provided in Table 2. Normalized mean bias (NMB) and correlation values are indicated in the top-left corner of each panel.

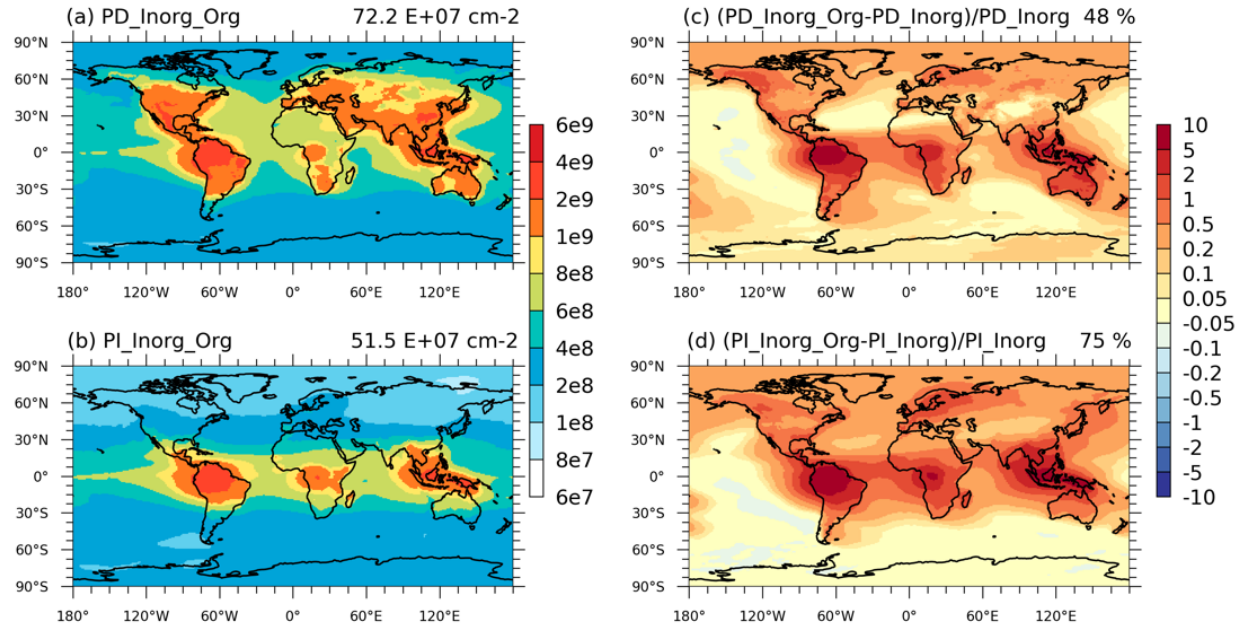

Figure S4. Spatial distribution of the simulated vertically-integrated aerosol number concentration in Aitken mode in **(a)** PD_Inorg_Org and **(b)** PI_Inorg_Org (unit: cm^{-2}). The relative change after adding organic NPF is shown in PD and PI environments are shown in **(c)** and **(d)**. Global mean values are shown on the top right of each figure.

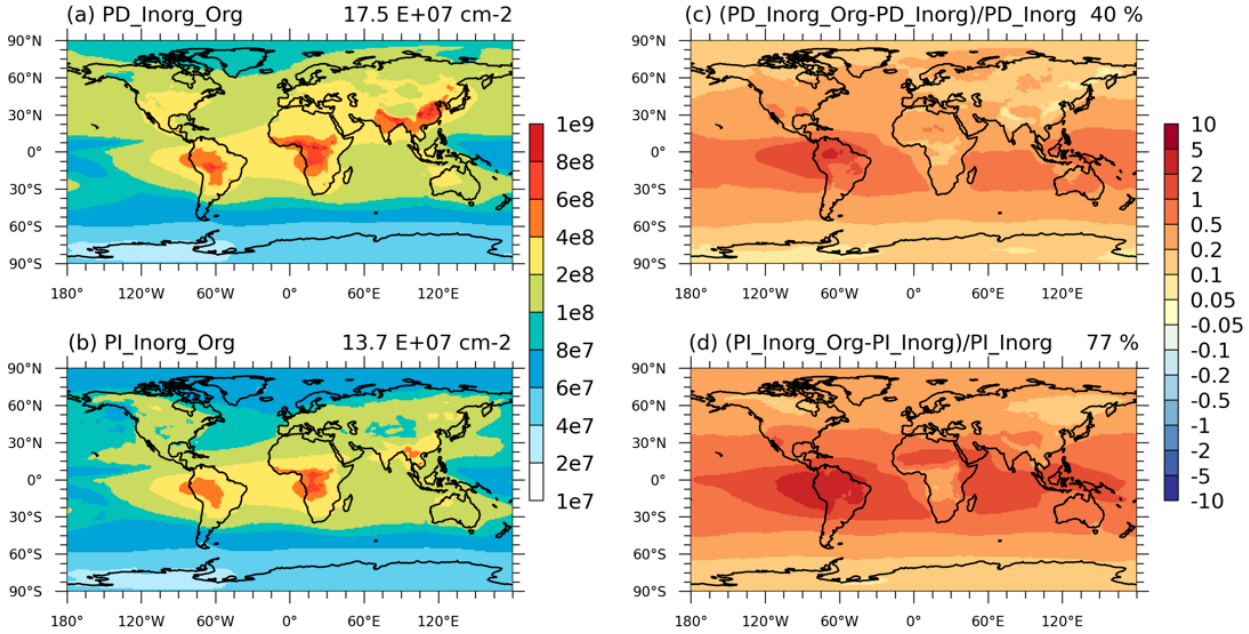

Figure S5. Spatial distribution of the simulated vertically-integrated aerosol number concentration in accumulation mode in **(a)** PD_Inorg_Org and (b) PI_Inorg_Org (unit: cm^{-2}). The relative change after adding organic NPF is shown in PD and PI environments are shown in **(c)** and **(d)**. Global mean values are shown on the top right of each figure.

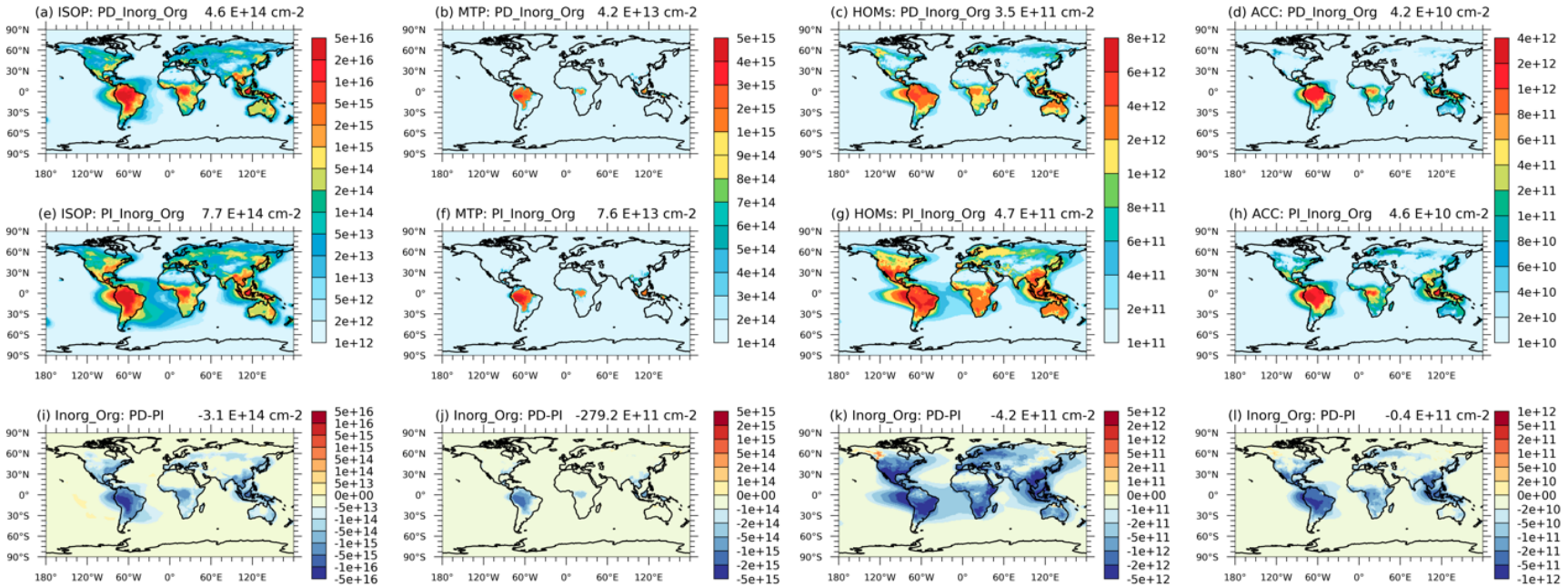

Figure S6. The Spatial distribution of the simulated vertically-integrated isoprene (ISOP) monoterpene (MTP), highly oxygenated organic molecules (HOMs), and accretion products (ACC) in PD_Inorg_Org **(a, b, c, and d)** and PI_Inorg_Org **(e, f, g, and h)** (unit: cm^{-2}). The differences in these variables between PD and PI environments is shown in **i, j, k, and l**. Global mean values are shown on the top right of each figure. Model experiments are described in **Table 2** and model data come from monthly mean value over 10 years.

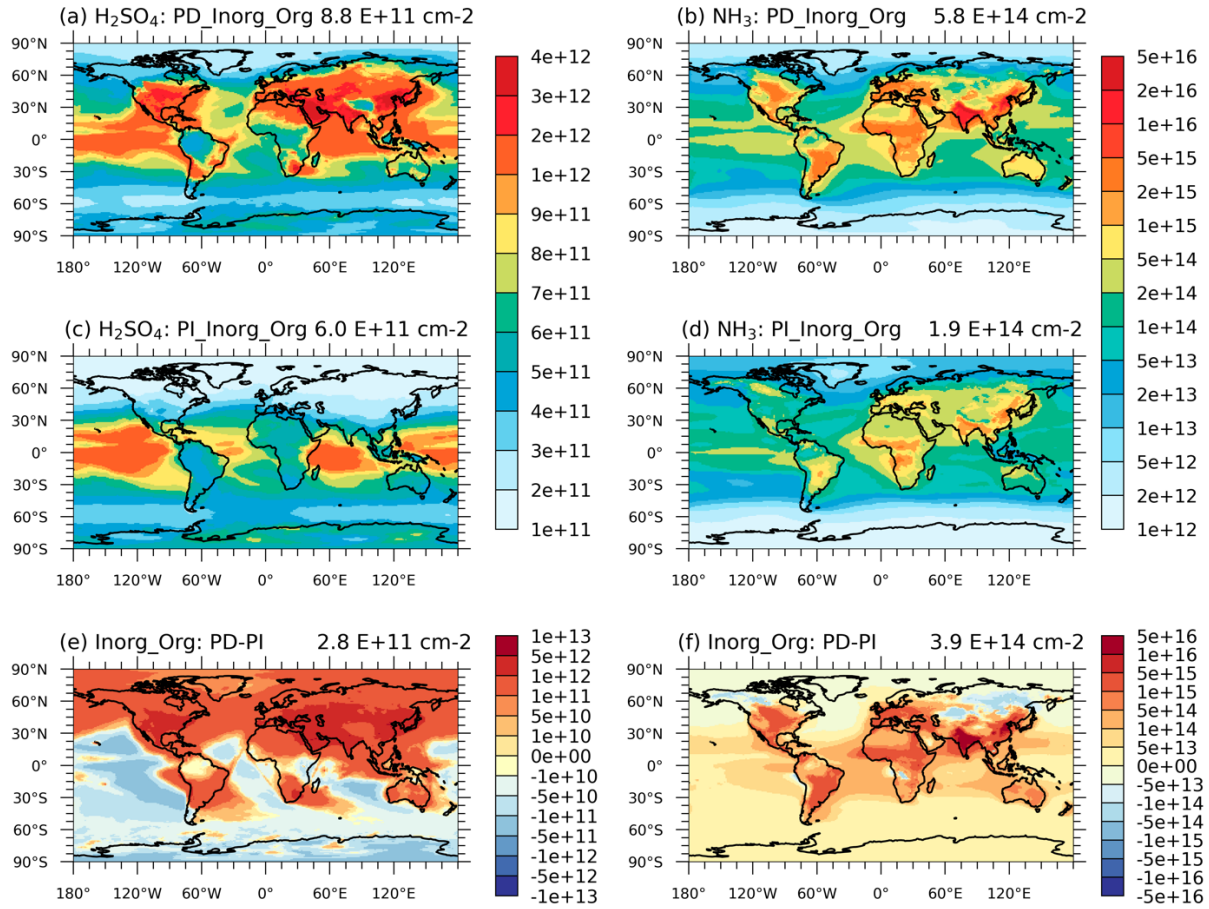

Figure S7. The Spatial distribution of the simulated vertically-integrated H_2SO_4 and NH_3 in PD_Inorg_Org **(a and b)** and PI_Inorg_Org **(c and d)** (unit: cm^{-2}). The differences in these variables between PD and PI environments is shown in **e and f**. Global mean values are shown on the top right of each figure. Model experiments are described in **Table 2** and model data come from monthly mean value over 10 years.

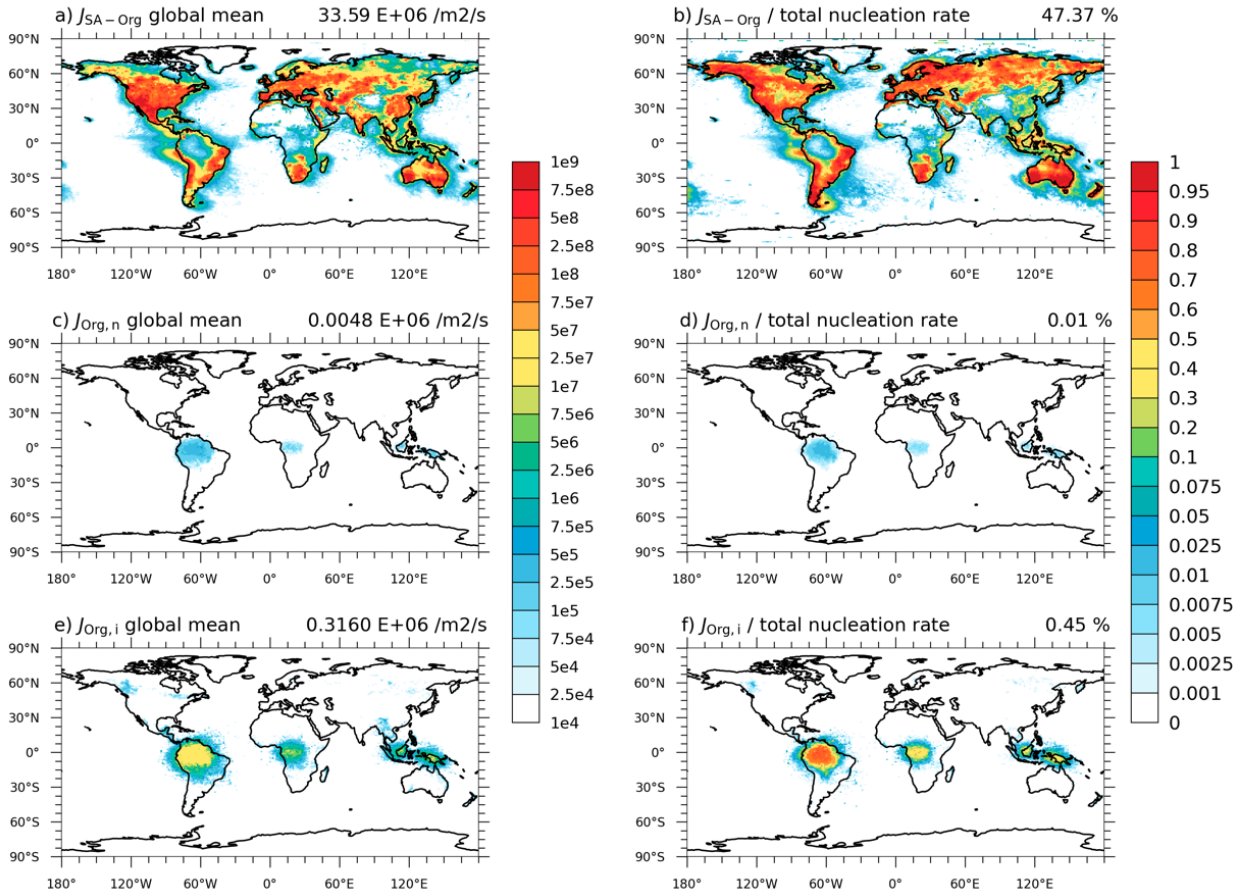

Figure S8. The vertically-integrated heteromolecular nucleation rate of sulfuric acid and organics ($J_{SA\text{-}Org}$) **(a)**, neutral pure organic nucleation rate ($J_{Org,n}$) **(c)**, and ion-induced pure organic nucleation ($J_{Org,i}$) **(e)** within the troposphere (unit: m^{-2} s^{-1}) and their contribution **(b, d, and f)** for total nucleation rate in the PD environment of the Inorg_Org case. Global mean values are shown on the top right of each figure. Model experiments are described in **Table 2** and model data come from monthly mean value over 10 years.

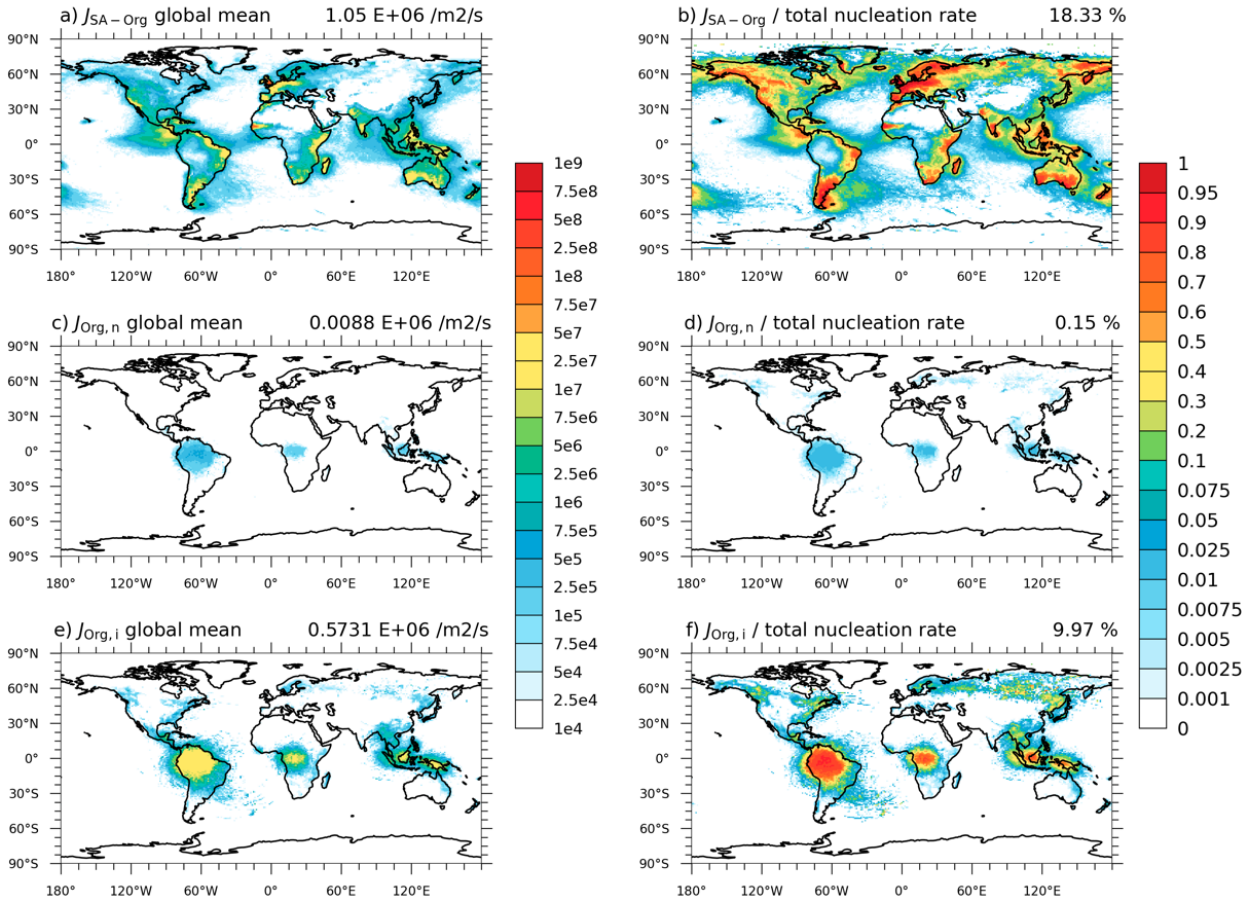

Figure S9. Same as **Figure S8**, but for PI environments.

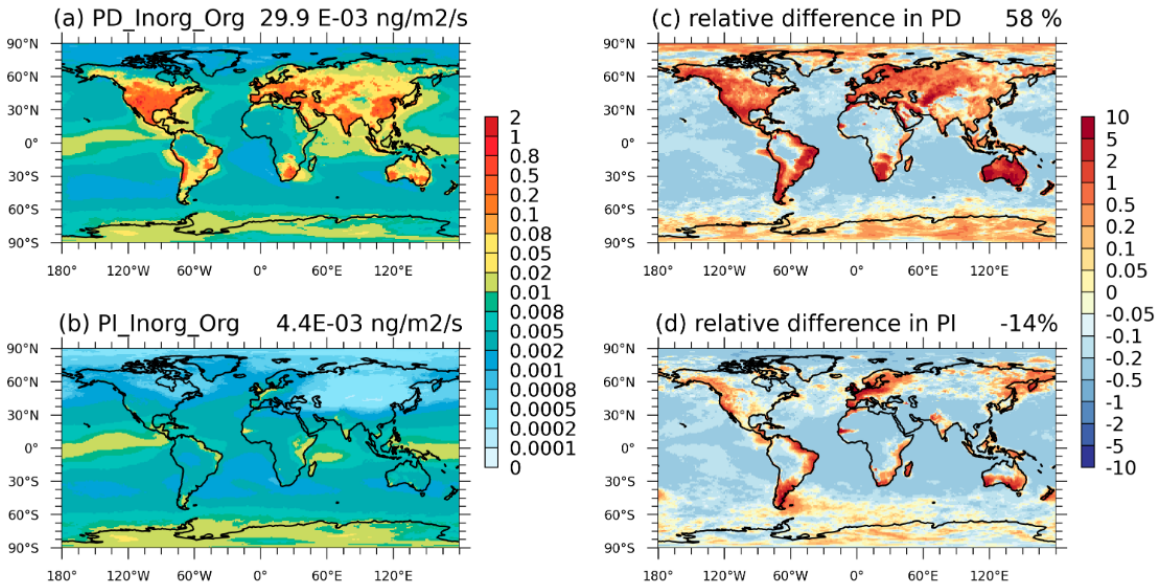

Figure S10. Spatial distribution of the simulated vertically-integrated sulfuric acid nucleation loss rate in (a) PD and (b) PI experiments (unit: ng m^{-2} s^{-1}). The relative difference between Inorg_Org and Inorg in PD and PI experiments is shown in (c) and (d) (unitless). Global mean values are shown on the top right of each figure.

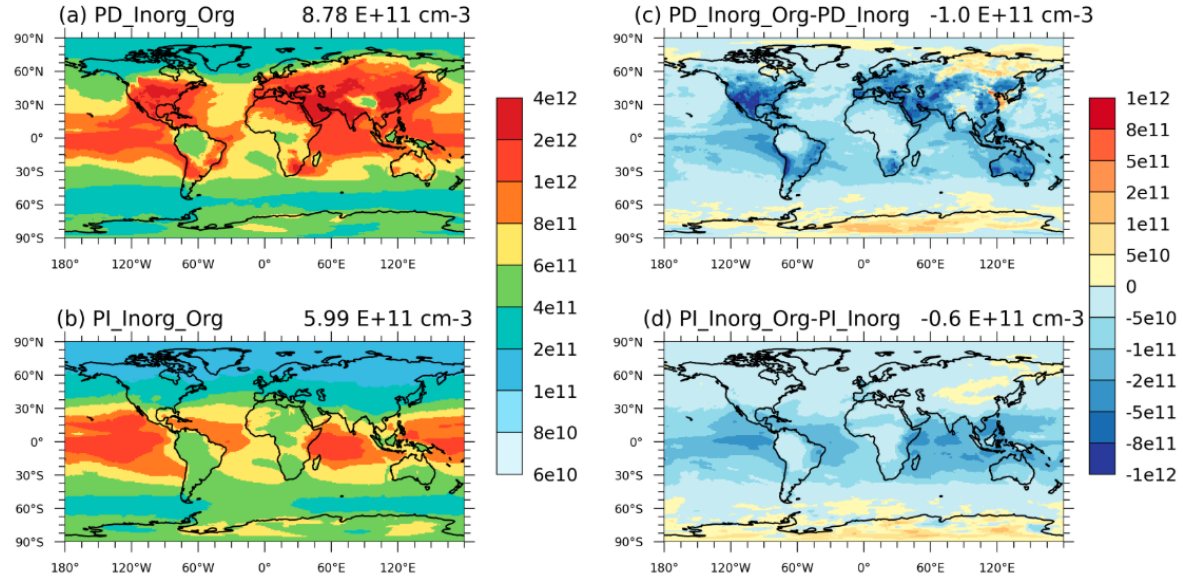

Figure S11. Spatial distribution of the simulated vertically-integrated sulfuric acid concentration in (a) PD and (b) PI experiments (unit: cm^{-2}). The difference between Inorg_Org and Inorg in PD and PI experiments is shown in (c) and (d) (unitless). Global mean values are shown on the top right of each figure.

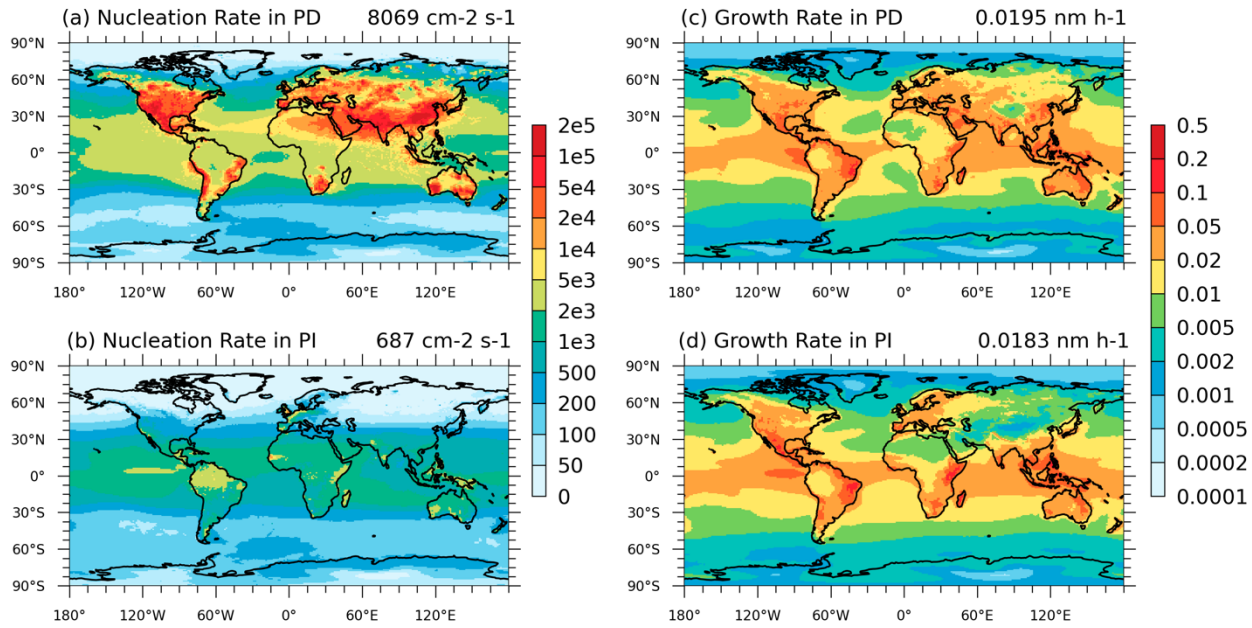

Figure S12. Spatial distribution of the simulated vertically-integrated nucleation rate (j1.7nm) in (a) PD_Inorg_Org and (b) PI_Inorg_Org (unit: cm-2 s -1). Spatial distribution of the simulated vertically-mean growth rate in PD_Inorg_Org (c) and (d). Global mean values are shown on the top right of each figure.

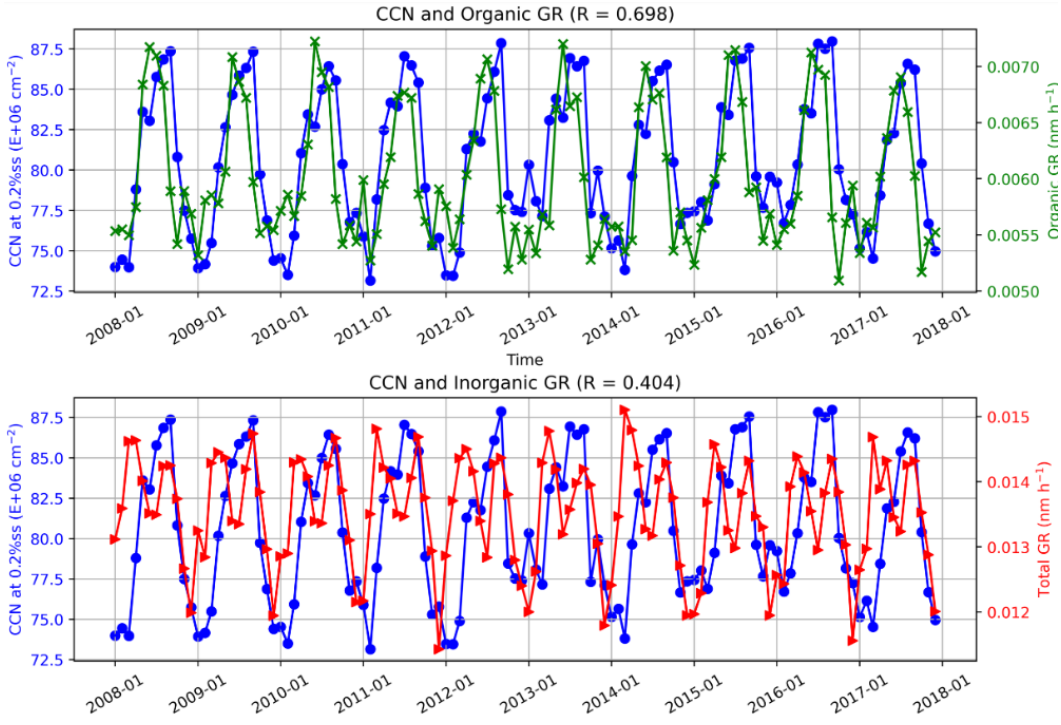

Figure S13. Global mean values of simulated CCN burden at 0.2% supersaturation (blue lines, unit: 10^6 cm^{-2}) and vertically averaged (a) organic and (b) inorganic growth rates (unit: nm h^{-1}) in the PD_Inorg_Org experiment. Pearson correlation coefficients between growth rates and CCN burden are shown in the titles of each panel.

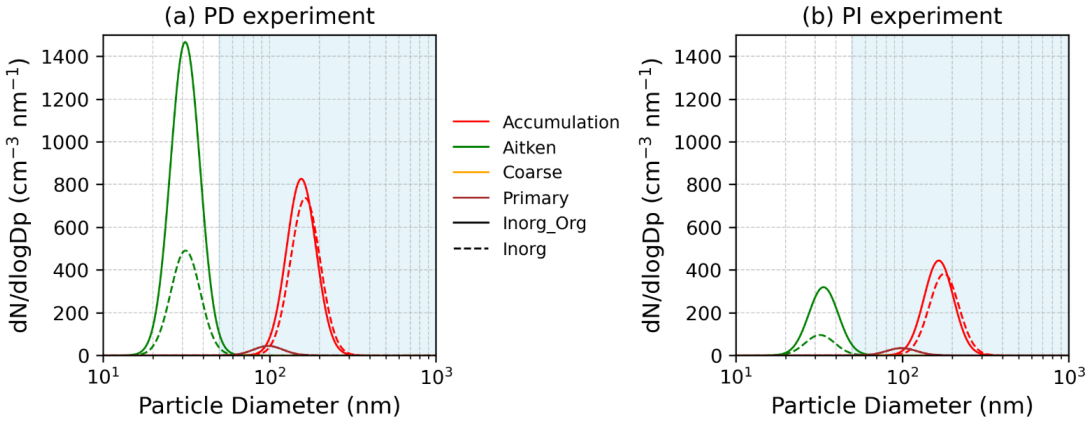

Figure S14. Particle number size distribution (PNSD) by mode in the (a) PD and (b) PI experiments. Solid lines represent the Inorg_Org simulation, and dashed lines represent the Inorg simulation. Each color corresponds to a specific mode: Accumulation (red), Aitken (green), Coarse (orange), and Primary (brown). The shaded blue area highlights particles with diameters larger than 50 nm, which are typically large enough to activate as CCN under ambient supersaturation conditions (Dusek et al., 2006).

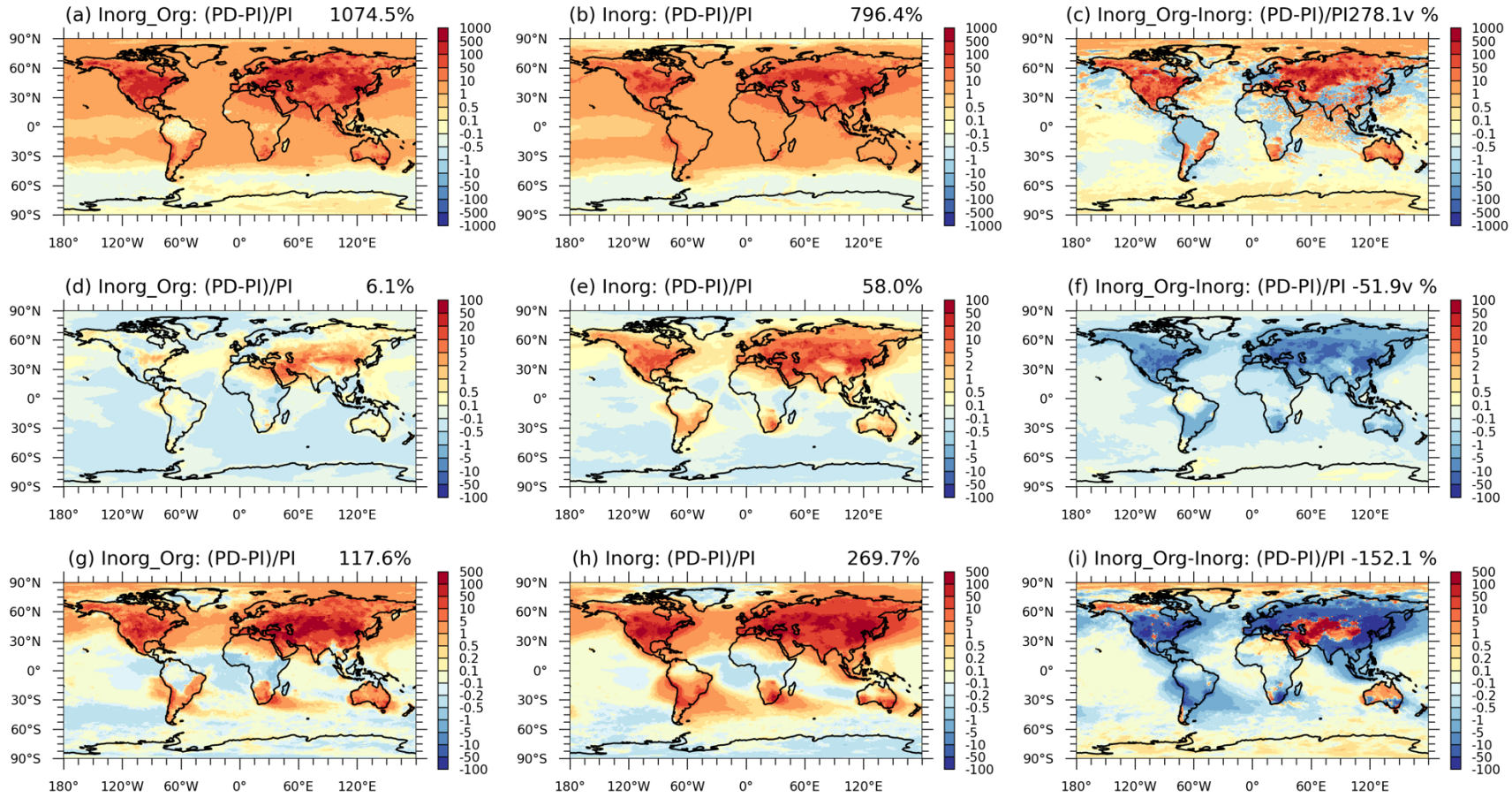

Figure S15. The relative change (unitless) of vertically-integrated nucleation rate ($j_{1.7nm}$), vertically-mean sub-20nm gorwth rate, and vertically-integrated apparent nucleation rate (j_{20nm}) in PD experiments comapred to PI environments (i.e., (PD-PI)/PI) in Inorg_Org **(a, d, and g)** and Inorg **(b, e, and h)**. The difference in the these variables between with and without organic NPF is shown in **c, f, and i**.

Table S3. Global mean of dry and wet deposition fluxes of different aerosols (including sulfate, secondary organic aerosol, primary organic matter and sea salt) in PD_Inorg_Org experiments. The PD fractional change ((PD-PI)/PI) of these variables in Inorg_Org and Inorg experiments are also shown. These aerosol sinks serve as proxies for CCN removal processes.

	Aerosol Type	Value	PD Fractional Change		
		PD_Inorg_Org ($ng\ m^{-2}\ s^{-1}$)	Inorg_Org	Inorg	Inorg_Org-Inorg
dry deposition flux	SO_4	0.82	25.4%	25.7%	-0.3%
	SOA	0.08	30.6%	32.2%	-1.6%
	POM	0.04	54.9%	32.2%	-1.6%
	Sea Salt	2.29	-2.4%	-2.5%	0.1%
wet deposition flux	SO_4	10.62	31.2%	30.1%	1.1%
	SOA	0.78	49.7%	48%	1.7%
	POM	0.78	74.5%	73.9%	0.7%
	Sea Salt	32.60	-0.1%	1.1%	-1.2%

Table S4. Decomposition of the global aerosol radiative forcing in different experiments ($W\ m^{-2}$).

	Inorg_Org ($W\ m^{-2}$)	Inorg ($W\ m^{-2}$)	Inorg_Org-Inorg ($W\ m^{-2}$)
Total effective aerosol forcing	-2.19	-2.64	0.45
Effective radiative forcing due to aerosol-cloud interactions (ERF_{aci})	-2.18	-2.59	0.41
Effective radiative forcing due to aerosol-radiation interactions (ERF_{ari})	0.03	-0.01	0.04